





**Magnetic-field-driven director configuration transitions in radial nematic liquid crystal droplets**Sophie Ettinger <sup>\*</sup>, Charlotte G. Slaughter , Sebastian Hurtado Parra, James M. Kikkawa,  
Peter J. Collings <sup>†</sup> and A. G. Yodh *Department of Physics and Astronomy, University of Pennsylvania, Philadelphia, Pennsylvania 19104, USA*

(Received 14 April 2023; accepted 21 July 2023; published 21 August 2023)

We study the director configurations of nematic liquid crystal (NLC) droplets with homeotropic anchoring in a magnetic field and report observation of a magnetic-field-driven transition from a deformed radial to an axial-with-defect configuration. Magnetic-field-induced transitions in NLC droplets differ fundamentally from the traditional planar Freedericksz transition due to the spherical droplet geometry and resulting topological defect. This transition has been studied theoretically, but the director configurations and mechanism of defect evolution in an applied magnetic field have yet to be observed experimentally. To this end, we combine polarized optical microscopy with a variable electromagnet ( $\leq 1$  T) for continuous observation of droplet director fields, and we employ Landau–de Gennes numerical simulations to elucidate the director configurations and first-order nature of the transition. We report a configuration transition from point defect to ring defect at a critical field, which varies inversely with droplet radius and is relatively independent of surfactant type and concentration. We also estimate anchoring strengths of commonly used surfactants at the NLC–aqueous interface.

DOI: [10.1103/PhysRevE.108.024704](https://doi.org/10.1103/PhysRevE.108.024704)**I. INTRODUCTION**

Nematic liquid crystals (NLCs) confined in spherical droplets exhibit a rich variety of director configurations resulting from the interplay of bulk elastic energy, surface anchoring energy, and defect structure. Transitions between these different director configurations and transformations of topological defects can be driven by changes in droplet size [1,2], boundary conditions [3], temperature [4–6], and external field. Notably, the radial to hyperbolic hedgehog director configuration transition was first explored experimentally and theoretically in response to temperature-induced changes in elastic constants in Ref. [4]. Here we study field-induced configuration transitions in NLC droplets. These transitions differ fundamentally from the classic Freedericksz transition in rectangular cells due to the presence of a geometrically enforced topological defect. Elucidation of this basic science provides essential insights about NLCs useful for the design of functional soft materials.

To date, experimental investigation of field-induced director configuration transitions in NLC droplets has been motivated by basic questions about the behavior of topological defects, as well as the possibility of applications, especially in polymer dispersed liquid crystal (PDLC) films. The vast majority of work has studied how electric fields affect either parallel anchoring-induced bipolar droplets [2,7–17] or perpendicular anchoring-induced radial droplets [2,8,18–21] dispersed in polymer matrices. More recently, the effect of electric fields on flat LC droplets has been investigated [22,23]. Both theory [8,18–20] and experiment [2,8,18–21]

report that at low electric fields, spherical PDLC droplets with homeotropic anchoring exhibit a gradual transformation from a radial to a “deformed radial” configuration with increasing electric field; here the point defect is preserved, and the surrounding director continuously reorients to align with the field. At a critical electric field, the PDLC droplets exhibit a discontinuous jump to an axial director configuration with a ring defect on the droplet surface.

The influence of magnetic fields on NLC droplets is less studied than that of electric fields. This is probably because NLC droplets in electric fields have more commercial applications. Director field responses of NLCs in magnetic fields, however, are much simpler than in electric fields. The magnetic anisotropy of NLC molecules causes their long axis to align with an external magnetic field. The same effect arises in electric fields, but since the dielectric anisotropy of most NLCs is large, complex internal fields can arise and reorganize in charge distribution on the NLC droplet surface, especially in aqueous solution, leading to inhomogeneous local fields. Use of magnetic fields ameliorates these complications and permits cleaner interpretation of the NLC response, since the director field is exclusively and directly dependent on the applied field.

Although the influence of magnetic fields on NLC droplets has been explored theoretically [24,25] as well as experimentally at low magnetic fields [26], significant unresolved questions remain concerning the resulting director configurations, defect structures, and nature of the transitions between configurations. At low magnetic field strength, Ref. [24] and Ref. [26] report a “deformed radial” configuration in which the director begins to align with the magnetic field while maintaining a predominately radial configuration and central point defect. At higher magnetic fields, all three studies describe a first-order configuration

<sup>\*</sup> [asophie@sas.upenn.edu](mailto:asophie@sas.upenn.edu)<sup>†</sup>Department of Physics and Astronomy, Swarthmore College, Swarthmore, PA, 19081, USA.

transition that occurs when the radial configuration with point defect is no longer stable [24–26].

Reference [24] predicts a critical field,  $H_c$ , at which the radial configuration becomes unstable, and a transition from point defect to ring defect occurs. When the surface anchoring strength is relatively weak, the droplet transitions to an axial configuration with a ring defect on the droplet surface; this phenomenon was observed experimentally for radial droplets in electric fields. When the anchoring strength is relatively strong, however, the droplet is predicted to transition first to an “axial-with-defect” configuration with ring defect *inside* the surface, i.e., in the bulk of the droplet. This transition state was neither reported for electric fields nor observed experimentally in magnetic fields. With further increase of magnetic field strength, the ring defect radius is predicted to increase until the axial configuration is achieved.

By contrast, Ref. [25] predicts a magnetic-field-induced transition from a radial configuration to an axial configuration, without intermediary states.<sup>1</sup> Reference [25] defines three critical fields: (1) the lower critical field where a metastable axial configuration first appears, (2) the thermodynamic critical field where the radial and axial configurations have the same free energy, and (3) the upper critical field, where the radial configuration becomes absolutely unstable. Experimentally, the transition is expected to be observed between the thermodynamic and upper critical field.

To date, no experimental studies have observed the radial to axial-with-defect transition in a magnetic field. Reference [26] defines a critical field, based on the experimental transmission pattern observed in polarized optical microscopy (POM), as when the extinction cross begins to gradually change shape to a “deformed radial” configuration. Although they do not observe the axial or axial-with-defect configurations predicted by theory, they suggest the point defect transforms into a ring defect in a first-order transition at much higher fields than were experimentally feasible.

In total, theoretical research on NLC droplets points to the fundamental importance of understanding magnetic-field-induced behavior on director fields containing topological defects, but the experimental studies are significantly lacking. In this contribution, we perform experiments and numerical simulations to investigate the director field evolution in NLC droplets in an applied magnetic field. We observe the deformed radial configuration, consistent with previous work [24,26], and we report the first experimental observation of the axial-with-defect configuration in a magnetic field, as predicted theoretically [24]. We identify a critical field  $H_c$  where a discontinuous, first-order transition from point defect<sup>2</sup> to

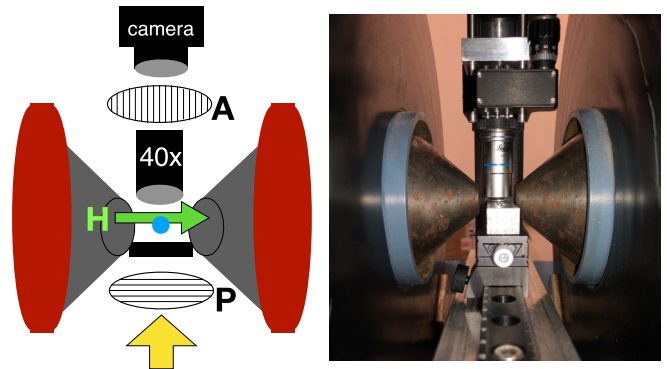


FIG. 1. Schematic (left) and photograph (right) of the experimental setup. Light enters the apparatus from the bottom (yellow arrow), passes through the first polarizer (P), the sample (blue circle), then the 40× objective, the analyzer (A), and, finally, it reaches the camera. The magnetic field ( $H$ , green) is generated by water-cooled Helmholtz coils with iron pole pieces that concentrate magnetic flux through the sample.

ring defect occurs, and we characterize its dependence on droplet radius and anchoring strength. Elucidation of these configuration transitions in NLC droplets provides physical insight about the competition between elastic energy, surface energy, and applied fields, which can be used for design of responsive NLC-based soft materials in magnetic fields.

## II. EXPERIMENTAL METHODS

To make the emulsions, 5  $\mu\text{l}$  of 5CB is hand-mixed with 100  $\mu\text{l}$  of surfactant solution. Shaking produces polydisperse droplets ranging in radius from 2 to 100  $\mu\text{m}$ . We fill borosilicate glass capillaries [Vitrocom,  $0.1 \times 1 \times 100$  mm or  $0.2 \times 1 \times 100$  mm (for larger droplets)] with the emulsion suspension for observation. All droplets displayed a radial hedgehog configuration in the absence of magnetic field and remained stable for days after generation.

We utilize a variety of surfactants including sodium dodecyl sulfate (SDS), sodium hexadecyl sulfate (SHS), dodecyltrimethylammonium bromide (C12TAB), myristyltrimethylammonium bromide (C14TAB), hexadecyltrimethylammonium bromide (C16TAB), and trimethyloctadecylammonium bromide (C18TAB). All surfactants are obtained from Sigma-Aldrich. The surfactant solutions of SDS, SHS, and nTAB contain concentrations below their critical micelle concentration (CMC), ranging from 5% to 60% of their CMC. To compare anchoring strengths of various surfactants, it is desirable that the amount of surfactant at the interface remains constant. We choose the concentration of each surfactant to be the same fraction of their CMC to achieve consistent interfacial excess concentrations. The CMC of the surfactants SDS, SHS, C12TAB, C14TAB, C16TAB, and C18TAB, respectively, is 8.25 mM [27], 0.2 mM [28], 15.0 mM [29], 3.83 mM [30], 1.0 mM [30], and 0.34 mM [31].

The experimental setup is pictured in Fig. 1. We use a tabletop Alpha Magnetics electromagnet to create a uniform  $\leq 1$  T magnetic field over the entire imaging area. The electromagnet is composed of a water-cooled Helmholtz coil with

<sup>1</sup>For all theoretical results, Ref. [25] assumes the ring defect in the axial configuration is located on the droplet surface. However, in practice, if the anchoring energy is large, then the ring defect may be separated from the surface by one magnetic coherence length ( $\sim 2$   $\mu\text{m}$ ).

<sup>2</sup>We refer to the central defect of a radial configuration as a point defect, although in experiment, this may be a ring defect, with a diameter comparable to the NLC defect core size. Note, these defects are topologically equivalent and do not change the first-order nature of the point-to-ring transition.

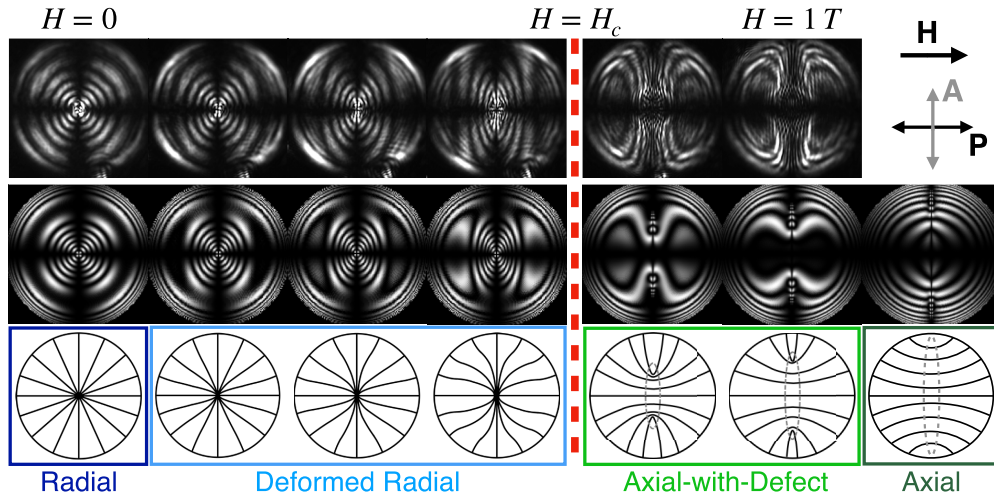


FIG. 2. Experimental POM images (top row), simulated POM images (second row), and schematics of the director configuration (bottom row) of a NLC droplet with homeotropic anchoring in a horizontal magnetic field of increasing strength. The droplet has a radius of  $25\ \mu\text{m}$ ; data are taken with 660-nm wavelength light. The director configuration schematics (bottom row) are drawn by following the director field lines obtained from LdG numerical simulation results. The first panel shows the radial configuration (dark blue box) at  $H = 0\ \text{T}$ . Panels 2–4 show a deformed radial configuration (light blue box). The red dashed line indicates the critical field  $H = H_c$ . Panels 5 and 6 show the axial-with-defect configuration (light green box), where the ring defect lies within the bulk of the droplet. The maximum magnetic field strength,  $H = 1\ \text{T}$ , is reached in panel 6. Panel 7 shows a simulated image of the quasiauxial configuration (dark green box), with ring defect approaching the droplet surface, which we do not observe in experiment.

a pair of truncated conical iron pole pieces that concentrate the magnetic flux by  $12\times$  to a  $1''$  diameter region. A Kepco 75-33 power supply (remote controlled via a GPIB interface) is employed to supply current to the electromagnet. The magnetic field strength at the sample position is measured with calibrated Hall sensors. For imaging, we engineered a custom microscope to fit within the electromagnet. We used IronCAD to design the structural components, which were fabricated in the University of Pennsylvania’s machine shop using aluminum, an effectively nonmagnetic material. The optical components and modular pieces are assembled using a ThorLabs 30-mm cage system.

The magnetic field is increased from 0 to 1.0 T in  $\sim 20$  minutes in increments of 0.01 T. Images are taken at each field increment; we wait 0.5 s after each field change before acquiring the image. This procedure ensured sample equilibration and field stability confirmed via Hall sensor readings. Imaging is performed using a  $40\times$  objective ( $\text{NA} = 0.66$ ) and a Kiralux 8.9 MP Monochrome CMOS camera from ThorLabs. The light source is a 4-Wavelength High-Power LED Source from ThorLabs, which is used to transmit either red light at 660 nm for monochromatic illumination or a combination of four wavelengths (470, 590, 617, and 660 nm) for broadband illumination. For each surfactant sample, we image 20–40 droplets, choosing droplets with a radial configuration and with minimal surfactant aggregates or water bubbles near the defect. Data are obtained in a temperature-controlled environment maintained at  $23\ ^\circ\text{C}$ . Data with temperature fluctuations larger than  $1\ ^\circ\text{C}$  are not used for analysis. The center of each droplet is determined using an image-correlation-based tracking algorithm.

Preliminary experiments revealed the same qualitative transition with gradual decrease in magnetic field. A detailed

analysis of hysteresis was not carried out in this study but is worth careful examination in future work.

### III. EXPERIMENTAL RESULTS: POM DATA

The top row of Fig. 2 shows exemplary POM snapshots of a  $25\ \mu\text{m}$  droplet as a function of increasing horizontal magnetic field ( $H$ ). The first panel at  $H = 0$  shows the radial configuration with the typical cross pattern associated with radial NLC droplets. Between crossed polarizers, a point defect appears as four dark brushes (horizontal and vertical) joined together at a point, such that transmitted light emerges as a bright lobe between each dark brush. In panels 2–4, when the magnetic field strength is relatively low but increasing, we observe the deformed radial configuration. This configuration evolves gradually and is first exemplified by asymmetry in the POM pattern. When the NLC aligns with the magnetic field, the spherical symmetry of the director configuration is broken. Due to phase retardation of light traveling through the NLC, the concentric circular fringes around the point defect contract horizontally and appear elliptical, with short axis parallel to the magnetic field. Importantly, in the deformed radial configuration, the director field in the droplet is distorted, but the point defect is not affected; therefore, the four bright lobes surrounding the point defect are preserved.

With further increase of the magnetic field, we reach the critical field,  $H = H_c$ , between panels 4 and 5 in the top row of Fig. 2, indicated by a red dotted line. The critical field is defined as the magnetic field at which the deformed radial configuration with a point defect transitions to an axial-with-defect configuration with a ring defect. The director field of the droplet gradually deforms as the magnetic

field increases but undergoes a critical transition at  $H_c$ . The defining characteristic of the transition is the replacement of a bright center surrounding the point defect with a dark region, indicative of an open ring. The ring defect expands with increasing magnetic field. The director field inside the ring defect is parallel to the magnetic field and thus parallel to a polarizer. In POM, this director configuration appears as a dark region in the center of the droplet, with two ellipsoidal lobes on the right- and left-hand sides of the droplet. The lobes are characterized by an asymmetrical shape outlined with bright fringes and a dark center.

As magnetic field strength is further increased, more of the NLC director aligns with the horizontal magnetic field. In POM, this produces a vertical expansion of the central dark region (panel 6 in the top row of Fig. 2). Due to homeotropic anchoring at the droplet surface, maximum alignment of the NLC occurs at the droplet center. Thus, the darkest areas of the droplet in POM are inside the ring defect and along the droplet equator, parallel to the magnetic field and polarizer. When we reach the maximum field strength of 1 T, the configuration is clearly in the axial-with-defect state.

To identify the critical field ( $H = H_c$ ) in POM, we carefully inspect the center of the droplet where the transition is most apparent. Since the phenomenon occurs in the vicinity of a point defect, the defining video frame for the transition is when the point defect appears to split (or open), and a dark center appears. Experimentally, this occurs more gradually than in simulation (see Sec. V). However, it is still possible to estimate a critical field at which the point defect disappears. This transition point is illustrated for various droplet sizes in Fig. 3. The critical field for each droplet is identified by eye using this visual cue. Other methods for identifying critical field were tested, including image analysis using ImageJ and Python. While there was reasonable agreement among all of the different analysis approaches, we found that identification of the critical field by eye was the most consistent and accurate method, likely due to the presence of thermal fluctuations of the nematic and slightly different cross patterns and image distortions associated with various droplet sizes. These effects increased the noise in the intensity data, making identification of the critical field more challenging for image software analyses. Details and examples of critical field identification using image software analysis are provided in Appendix A.

#### IV. SIMULATION METHODS

We use the standard  $Q$ -tensor-based Landau-de Gennes (LdG) numerical model [32,33] to simulate relaxation of a NLC in a spherical confinement. The free energy is minimized in a finite difference scheme on a regular cubic mesh using a conjugate gradient algorithm from the ALGLIB [34] package. The open-source version of this code is available online and is described in detail in Ref. [35].

In the uniaxial limit, the LdG free energy is written in terms of the tensor  $\mathbf{Q}_{ij} = \frac{3}{2}S(\mathbf{n}_i\mathbf{n}_j - \frac{1}{3}\delta_{ij})$ , where  $\mathbf{n}_i$  is the  $i$ th component of the nematic director,  $\delta_{ij}$  is the Kronecker delta, and  $S$  is the nematic order parameter. The nematic director can be recovered from  $\mathbf{Q}$  as the eigenvector corresponding to the largest eigenvalue,  $S$ . We use  $S = 0.53$  [32,36]. The LdG free energy density is the sum of the background phase free energy

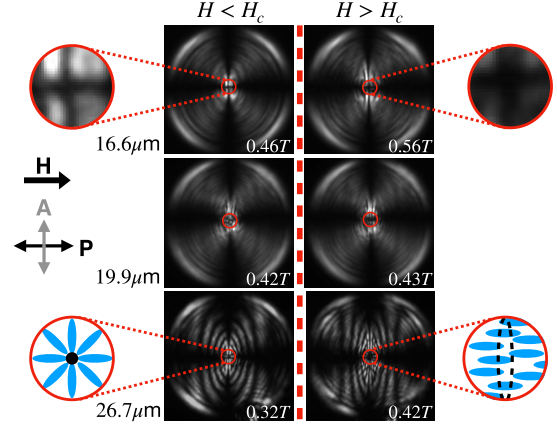


FIG. 3. Experimental POM images of three different droplets before and after the configuration transition critical field. The droplets are 16.6, 19.9, and 26.7  $\mu\text{m}$  in radius from top to bottom. The top two rows show experimental data using white light, and the bottom row shows experimental data using 660-nm wavelength light. The left column shows the droplet immediately before the transition in the deformed radial state with a point defect. After the transition, the right column shows the droplet in the axial-with-defect state. The red circle is a guide to the eye which highlights the region we examine to identify the critical magnetic field. The top insets show a magnified view of the POM image inside the red circle. The bottom insets show a simplified schematic of the defect before and after the transition, where the blue ovals represent the NLC mesogens. The black point and dashed line indicate the point and ring defect, respectively. The field strength corresponding to each frame is displayed on the image. The magnetic field is horizontal, and the black and gray arrows indicate the orientation of the polarizer and analyzer.

density and the distortion free energy density:

$$f_{\text{LdG}} = f_{\text{phase}} + f_d. \quad (1)$$

The phase free energy density is as follows:

$$f_{\text{phase}} = \frac{A}{2}\text{Tr}(\mathbf{Q}^2) + \frac{B}{3}\text{Tr}(\mathbf{Q}^3) + \frac{C}{4}[\text{Tr}(\mathbf{Q}^2)]^2, \quad (2)$$

where  $\text{Tr}$  is the trace. We use the LdG parameters of 5CB,  $A = (-0.172 \times 10^6) \text{ J/m}^3$ ,  $B = (-2.12 \times 10^6) \text{ J/m}^3$ , and  $C = (1.73 \times 10^6) \text{ J/m}^3$  [32]. The distortion free energy density using all three elastic constants is

$$f_d = \frac{L_1}{2} \frac{\partial Q_{ij}}{\partial x_k} \frac{\partial Q_{ij}}{\partial x_k} + \frac{L_2}{2} \frac{\partial Q_{ij}}{\partial x_j} \frac{\partial Q_{ik}}{\partial x_k} + \frac{L_3}{2} Q_{ij} \frac{\partial Q_{kl}}{\partial x_i} \frac{\partial Q_{kl}}{\partial x_j}. \quad (3)$$

This is the LdG counterpart to the Frank-Oseen free energy:

$$f_{\text{Frank}} = \frac{K_{11}}{2} (\nabla \cdot \mathbf{n})^2 + \frac{K_{22}}{2} [\mathbf{n} \cdot (\nabla \times \mathbf{n})]^2 + \frac{K_{33}}{2} |\mathbf{n} \times (\nabla \times \mathbf{n})|^2, \quad (4)$$

where  $K_i$  are the Frank elastic constants as combinations of  $L_i$  [32]. We use reported splay ( $K_{11} = 6.4 \text{ pN}$ ), twist ( $K_{22} = 4.0 \text{ pN}$ ), and bend ( $K_{33} = 8.4 \text{ pN}$ ) elastic constants for 5CB [37,38]. The simulation also takes  $K_{24} = K_{22}$ .

We simulate a droplet in a box size of  $264 \times 264 \times 264$  units, with a mesh size of  $\Delta x = 5 \text{ nm}$ . The droplet has a radius

of 130 grid units, and the region outside the droplet is not simulated. For all simulations, we use a small colloid one grid unit in radius in the center of the droplet to stabilize the radial configuration with a point defect at zero field. For nonzero fields, the small colloid has an effect in a region only one grid unit next to the colloid, thus representing a very small contribution to the free energy calculation. At the critical field, a  $+\frac{1}{2}$  ring disclination forms at about half the drop radius, and a  $-\frac{1}{2}$  ring disclination forms one grid unit outside the colloid.

The boundary free energy is modeled using a Rapini-Papoular surface potential [39], and the droplet surface as well as the central colloid has homeotropic anchoring of strength  $1 \times 10^{-3} \text{ J/m}^2$ . The difference in experimental and simulation anchoring strength is due to the significantly different scale between experiment and simulation. The director field is initialized randomly. The magnetic field is uniform in space and applied along the  $x$  axis of the droplet and ranges from 0 to 100 mT. We use the literature value of  $\chi_a$  for 5CB,  $1.56 \times 10^{-6}$  [40].

To connect numerical results with experiment, we generate simulated POM images by performing Jones matrix calculations with the computed three-dimensional nematic. The indices of refraction of 5CB are  $n_e = 1.70$  and  $n_o = 1.55$  [41].

## V. SIMULATION RESULTS

To further corroborate the experiment and understand the director configurations of droplets with homeotropic anchoring in a magnetic field, we perform simulations using a LdG numerical model.

At zero field, the equilibrium configuration is a radial configuration. Applying a relatively low uniform magnetic field along one axis distorts the radial configuration while maintaining a point defect at the center. This is the “deformed radial” configuration. Schematics of the simulated radial and deformed radial director configurations are shown in the bottom row of Fig. 2. These schematics are constructed by drawing continuous lines over director field data from simulation. At a critical field, the simulated droplet transitions from a radial configuration to an axial-with-defect configuration (“Axial-with-Defect” schematic in Fig. 2). Above the critical field, the ring defect radius increases with increasing magnetic field strength. Finally, when the field strength is sufficiently large, the director field in the droplet aligns almost entirely with the magnetic field, approaching the axial configuration (“Axial” schematic in Fig. 2). The strong anchoring boundary conditions of the simulation do not allow a true axial configuration to form, and therefore we refer to the director configuration at high magnetic fields in simulation as a quasiaxial configuration. Repeated simulations with varying anchoring strengths show the same intermediate director configurations at different field strengths (stronger anchoring leads to higher critical fields).

We use Jones calculus to generate POM images for comparison to experiment from the three-dimensional (3D) director field simulation results. These images are presented in the middle row of Fig. 2. Note that we did not observe the axial configuration in experiment due to our limited magnetic field strength. However, we can predict the POM texture using the quasiaxial configuration from simulation. Comparing the

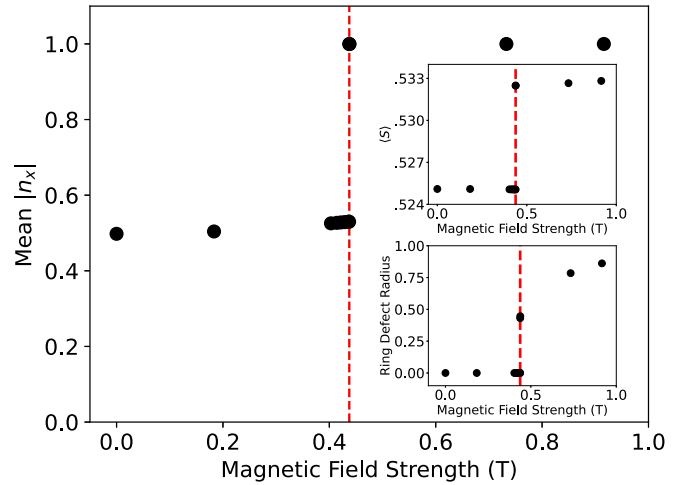


FIG. 4. Mean value of  $|n_x|$  (absolute value of  $x$  component of director field) from the LdG simulation in a small region surrounding the defect as a function of magnetic field strength. Top inset shows mean order parameter ( $\langle S \rangle$ ) in this same region. Bottom inset shows ring defect radius (scaled by droplet radius) calculated using LdG simulation director field results. Order parameter ( $S$ ) and  $|n_x|$  are averaged over a sphere of radius  $r/8$ , which lies inside the smallest ring defect. For all plots, the red dashed line indicates critical field.

experimental images in the top row of Fig. 2 to the simulation images in the middle row, we see that the images match extremely well. In particular, the number of fringes remains the same from  $H = 0$  to  $H = H_c$ , and the fringes contract horizontally with increasing field. The dark areas on either side of the circular or ellipsoidal fringes appear quite similar in both simulation and experiment and grow with increasing field. For field strengths above the transition, the dark center region becomes visible and expands with increasing field.

Some discrepancies between the simulation and experimental images are apparent in the axial-with-defect state; they are visible along the vertical axis of the droplet. These differences may be due to the limited resolution of the simulations, which leads to a blurring together of numerous thin fringes or due to optical effects such as refraction at the LC-aqueous interface, which are neglected by the Jones matrix calculation (consistent with assumptions employed previously and demonstrated to be reasonable for large droplets with modest birefringence [42]). The ring defects in the two axial-with-defect configurations are 60% and 70% of the droplet radius, respectively, providing an estimate of the ring defect size in the two experimental images above  $H_c$ . Figure 4 also provides a prediction for the maximum ring defect size achieved in experiment: approximately 85% of the droplet size.

We also use LdG simulation to calculate the average order parameter and director field components in a region surrounding the defect to characterize the nature of the transition. Figure 4 shows the mean order parameter ( $\langle S \rangle$ ) and mean absolute value of the  $x$  component of the director ( $\langle |n_x| \rangle$ ) in a small sphere surrounding the defect as a function of increasing magnetic field strength. The sphere has a radius  $r/8$ , and lies inside the smallest ring defect. Note that both

these measurements exclude the central defect and its nearest-neighbor points (see Sec. IV). The discontinuous jump in  $\langle S \rangle$  and  $\langle |n_x| \rangle$ , which occurs at the transition from point defect to ring defect, suggests this phenomenon is a first-order transition. The lower inset of Fig. 4 presents the ring defect radius in simulation as a function of magnetic field strength. The radius of the smallest axial-with-defect disclination ring is approximately half the droplet radius. This further suggests that the transition occurs as a discontinuous jump from point defect to ring defect at the critical field. Additional evidence of discontinuous parameters in simulation, such as image intensity analysis, is presented in Appendix A.

Due to the topological defect required by droplet geometry and surface anchoring, the simulation is not scale free. Defect core size does not scale with system size, which can lead to discrepancies between numerical results and experimental observation, especially when comparing values of  $H_c$ . Because of these limitations, we use numerical simulations to visualize the 3D director field in prototypical configurations rather than to determine critical field values. For comparison purposes, the magnetic field strength in the simulation and plotted in Fig. 4 is scaled to the experimental range using the ratio of the experimental and simulated droplet radii.

## VI. EXPANDING RING MODEL: CALCULATION AND EXPERIMENTAL COMPARISON

We use analytical modeling to explore an alternative possibility that experimental droplets begin with a very small ring defect (i.e., approximately the size of the defect core) that gradually expands with increasing magnetic field strength. This possibility is to be contrasted with the discontinuous transition found using LdG simulation (critical field model). We call this scenario the expanding ring model. In this case, a gradual increase in ring defect size occurs (proportional to magnetic field strength) and there is no critical transition. To determine the 3D director field for all possible ring defect radii, we perform an analytical calculation to obtain a 3D director field for all ring defect radii and use Jones calculus to generate POM images from simulation results which can be compared to experimental observations.

Following Ref. [25], we model the director field using ellipsoidal coordinates  $\sigma$ ,  $\tau$ , and  $\phi$ , with the assumption that

the director field follows lines of constant  $\tau$ . By rotating the configuration around its axis of symmetry, we adapt this model to three dimensions using prolate spheroidal coordinates, wherein the director follows surfaces of constant  $\tau$ .

We start with the alternative definition of prolate spheroidal coordinates:

$$x = a\sqrt{(\sigma^2 - 1)(1 - \tau^2)} \cos \phi, \quad (5)$$

$$y = a\sqrt{(\sigma^2 - 1)(1 - \tau^2)} \sin \phi, \quad (6)$$

$$z = a\sigma\tau, \quad (7)$$

where  $a$  is the ring defect radius. Using Mathematica, we calculate the derivative of  $x$ ,  $y$ , and  $z$  with respect to  $\sigma$  and  $\phi$  along lines of constant  $\tau$  to obtain  $dx$ ,  $dy$ , and  $dz$ . These are normalized to obtain the director field components  $n_x$ ,  $n_y$ , and  $n_z$  in terms of the prolate spheroidal coordinates:

$$n_x = s\sqrt{\frac{-1 + \tau^2}{-\sigma^2 + \tau^2}} \cos \phi, \quad (8)$$

$$n_y = s\sqrt{\frac{-1 + \tau^2}{-\sigma^2 + \tau^2}} \sin \phi, \quad (9)$$

$$n_z = t\sqrt{\frac{-1 + \sigma^2}{\sigma^2 - \tau^2}}. \quad (10)$$

In order to convert the director field to Cartesian coordinates, we solve Equations (5)–(7) for  $\sigma$ ,  $\tau$ , and  $\phi$  in terms of  $x$ ,  $y$ ,  $z$ , and  $a$ :

$$\sigma = \frac{1}{2a}[\sqrt{x^2 + y^2 + (z + a)^2} + \sqrt{x^2 + y^2 + (z - a)^2}], \quad (11)$$

$$\tau = \frac{1}{2a}[\sqrt{x^2 + y^2 + (z + a)^2} - \sqrt{x^2 + y^2 + (z - a)^2}], \quad (12)$$

$$\phi = \arctan(y/x). \quad (13)$$

Finally, we substitute these into Eqs. (8)–(10) to give the  $x$ ,  $y$ , and  $z$  components of the director field for any given ring defect radius  $a$ ,

$$n_x = \frac{x}{\sqrt{2}\sqrt{x^2 + y^2}} \sqrt{\frac{x^2 + y^2 - z^2 - a^2}{\sqrt{(x^2 + y^2 - a^2)^2 + 2z^2(x^2 + y^2 + a^2)} + z^4}} + 1, \quad (14)$$

$$n_y = \frac{y}{\sqrt{2}\sqrt{x^2 + y^2}} \sqrt{\frac{x^2 + y^2 - z^2 - a^2}{\sqrt{(x^2 + y^2 - a^2)^2 + 2z^2(x^2 + y^2 + a^2)} + z^4}} + 1, \quad (15)$$

$$n_z = \frac{1}{\sqrt{2}} \sqrt{\frac{-x^2 - y^2 + z^2 + a^2}{\sqrt{(x^2 + y^2 - a^2)^2 + 2z^2(x^2 + y^2 + a^2)} + z^4}} + 1. \quad (16)$$

We can then use Jones calculus to generate a POM image from the 3D director field results, presented in the second row of Fig. 5, which can be compared to the experimental data, reproduced from Fig. 2 in the top row of Fig. 5.

Focusing on the simulated POM images in Fig. 5 (second row), the radial configuration in Fig. 5 uses the same image as the radial configuration in the critical field model (Fig. 2). The axial-with-defect configurations in the fifth and sixth panels of

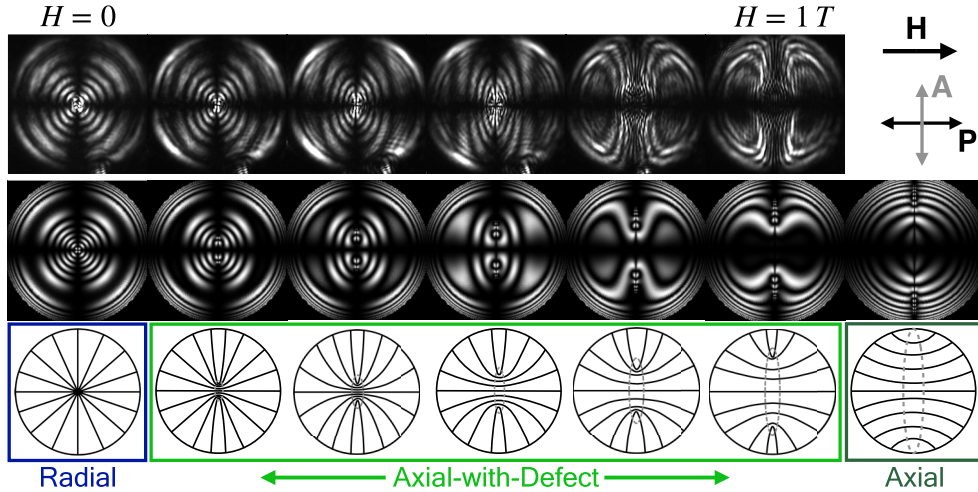


FIG. 5. Top row shows experimental POM images of the director configuration evolution of an NLC droplet with homeotropic anchoring in an increasing horizontal magnetic field (identical to Fig. 2). The droplet is 25  $\mu\text{m}$  in radius; data are taken with 660-nm wavelength light. The second row shows simulated POM images generated by performing Jones matrix calculus on the 3D director field modeled using prolate spheroidal coordinates, assuming the expanding ring model described in Sec. VI. Schematics (bottom row) are drawn by following director field lines resulting from analytical calculation. The first panel shows the radial configuration at  $H = 0$  (dark blue box). Panels 2–6 show an axial-with-defect configuration (light green box), where the ring defect radius increases with magnetic field strength. The maximum magnetic field strength,  $H = 1 \text{ T}$ , is reached in panel 6. Panel 7 shows a simulated image of the axial configuration (dark green box), which we do not observe in experiment.

Fig. 2 and Fig. 5 are also identical. We thus focus on the only differing configurations, panels 2–4, to compare the two possible paths of evolution. In these panels, the critical field model (Fig. 2) predicts a deformed radial configuration, while the expanding ring model (Fig. 5) predicts an axial-with-defect configuration. One important characteristic differentiates the two models. In the expanding ring model (Fig. 5), the number of fringes surrounding the center decreases throughout panels 2–4, while the number of fringes remains constant in the critical field model (Fig. 2). Clearly, the point-to-ring transition (critical field model) matches the experimental data much more closely. This comparison thus provides further evidence that the transition from point to ring defect at the critical field is discontinuous and first-order in nature.

**VII. CRITICAL FIELD MODELS**

Our experimental and simulated data together show that a radial NLC droplet in a magnetic field discontinuously transitions to an axial-with-defect configuration at critical field  $H_c$ . To quantitatively explore this behavior further, and to estimate interfacial anchoring strength, we employ two models that quantify the relationship between critical magnetic field, droplet radius,  $r$ , and anchoring strength,  $W$ . The first model employs the classic Freedericksz transition equation for a rectangular cell of NLC in a magnetic field; the second model employs the saturation field equation for weak boundary conditions, as proposed by Ref. [43] for a rectangular cell of NLC in an electric field. In Appendix B, we discuss both models, evaluate the accuracy of each model in characterizing the point-to-ring defect transition, and present interfacial anchoring strength estimates for a variety of surfactants and concentrations based on our measurements and the two models.

Anchoring strength measurements for SDS, SHS, and nTAB using both the Freedericksz transition model and the saturation field model are reported in Table I. Within experimental error, we find that interfacial anchoring strength is largely independent of surfactant concentration and chain length. We also find that SDS, SHS, and nTAB surfactants have similar anchoring strengths, with a weighted average value of  $4.68 \times 10^{-6} \text{ J/m}^2$ , using the Freedericksz transition model. A collapse of all experimentally measured critical field

TABLE I. Experimentally measured anchoring strengths for all surfactant samples using both models of critical field analysis: the Freedericksz transition model and the saturation field model.

Surfactant sample	Anchoring strength, $W$	Anchoring strength, $W$
	Freedericksz transition model ( $\text{J/m}^2$ )	saturation field model ( $\text{J/m}^2$ )
C12TAB 10% CMC	$5.86 \pm 3.75$	$1.29 \pm 0.23$
C14TAB 10% CMC	$4.72 \pm 3.07$	$1.10 \pm 0.20$
C16TAB 5% CMC	$4.18 \pm 1.81$	$1.25 \pm 0.23$
C16TAB 10% CMC	$5.90 \pm 4.15$	$1.20 \pm 0.20$
C16TAB 15% CMC	$3.66 \pm 1.52$	$1.36 \pm 0.26$
C16TAB 20% CMC	$6.27 \pm 5.62$	$1.08 \pm 0.18$
C18TAB 10% CMC	$6.23 \pm 3.55$	$1.52 \pm 0.27$
SDS 5% CMC	$4.58 \pm 2.15$	$1.32 \pm 0.22$
SDS 10% CMC	$4.71 \pm 1.67$	$1.34 \pm 0.24$
SDS 15% CMC	$7.50 \pm 4.67$	$1.44 \pm 0.24$
SDS 20% CMC	$4.37 \pm 1.82$	$1.35 \pm 0.24$
SDS 40% CMC	$5.94 \pm 3.42$	$1.37 \pm 0.23$
SDS 60% CMC	$4.86 \pm 2.08$	$1.37 \pm 0.24$
SHS 10% CMC	$5.37 \pm 2.96$	$1.40 \pm 0.24$

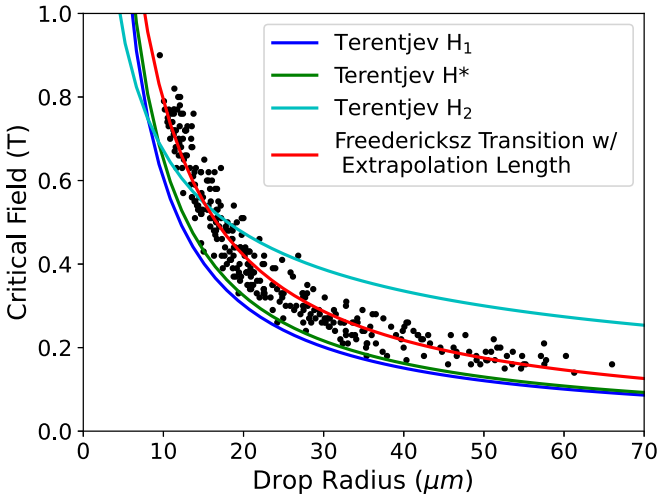


FIG. 6. Experimentally observed critical field values (black points) versus drop radius for all surfactant (SDS, SHS, or nTAB) samples. The fit lines correspond to the three critical field equations from Ref. [25], as well as the Freedericksz transition equation model in red. The three critical fields of Ref. [25] are, respectively, the lower critical field where a metastable axial state first appears (blue curve), the thermodynamic critical field where both the radial and axial states have the same free energy (green curve), and the upper critical field, where the radial configuration becomes absolutely unstable (cyan curve). The Freedericksz transition model (red curve) uses the average anchoring strength found from fitting,  $W = 4.68 \times 10^{-6} \text{ J/m}^2$ .

data points, for all surfactants and concentrations, is shown in Fig. 6. The overall collapse onto a single curve highlights our conclusion that SDS, SHS, and nTAB have comparable anchoring strengths.

### VIII. DISCUSSION

The experimental and simulated data together show that a radial NLC droplet undergoes a configuration transition in an applied magnetic field. At low fields, the radial director field gradually deforms to align with the magnetic field while preserving the point defect in a deformed radial configuration. At a critical magnetic field, the point defect becomes unstable and abruptly transitions into a ring defect, with ring axis parallel to the field. This is the axial-with-defect configuration, wherein the ring defect lies within the bulk of the droplet. Above the critical field, the ring defect expands with magnetic field strength, an effect we observe in both experiment and simulation. The simulations further show that the ring defect grows with field strength until it approaches the droplet surface in a quasiaxial configuration at very large magnetic fields.

Taken together, our simulations and our comparison of experiment with analytic modeling suggest that this configuration transition is first order, consistent with theoretical predictions [24,25]. Specifically, POM images modeling a gradual ring expansion clearly differ from experimental POM images, and the jump in order parameter, director components, and ring defect radius in simulation all show a discontinuity at the critical field, further suggesting that the transition is first order.

This work is the first experimental observation of a magnetic-field-driven transition from a radial to an axial-with-defect configuration. Reference [26] also examined radial droplets in a magnetic field experimentally but did not observe the radial to axial-with-defect transition due to the use of much lower magnetic field strengths ( $\leq 0.15 \text{ T}$ ). Since they only observed the radial and deformed radial configuration, in their paper they defined a critical field between these two states. By contrast, the critical magnetic field described by Ref. [25] and Ref. [24] agrees with our observations: a first-order transition from a point defect to a ring defect.

Beyond observation of this primary transition feature, our study has both qualitative differences and similarities with respect to the director configuration predictions of theoretical work [24,25]. Our observation of two intermediary stages between the radial and axial configuration is in agreement with Ref. [24] but disagrees with Ref. [25], which describes a transition from a pure radial configuration directly to an axial configuration. This can be attributed to the latter's assumption that the director field follows coordinate lines of the ellipsoidal coordinate system. A deformed radial configuration is not possible with this analytical ansatz. In addition, Ref. [25] assumes the droplet interface has infinitely strong anchoring, while the anchoring strengths in our experiments are comparatively weak. In Fig. 6, we compare our data and Freedericksz transition model to the critical field equations of Ref. [25]. We plot the Freedericksz transition model for our experimental data (using our estimated  $W = 4.68 \times 10^{-6} \text{ J/m}^2$ ). While the four curves are quite similar, we find that the Freedericksz transition model with finite anchoring best describes our experimental data. Notably, the Freedericksz transition model critical field curve lies between the thermodynamic critical field and the upper critical field, which is where Ref. [25] predicts the critical field should occur experimentally.

The configuration evolution we observe experimentally is consistent with predictions in the *strong anchoring* regime of Ref. [24]. In Fig. 7, we compare our experimental results to the phase diagram from Ref. [24] (using our estimated anchoring strength,  $W$ ). For clarity, the phase diagram from Ref. [24] is reproduced with color, and our experimental results are overlaid using the same dimensionless axes. Note that the radial region in this diagram is characterized by a point defect and includes the deformed radial configuration. Both our experimental data and the theoretical curves show that the critical field increases with decreasing droplet size. The main difference between experiment and theory is that Ref. [24] predicts a transition from radial to axial configuration at values of  $\mu$  within our experimental range. Our experiments, by contrast, show a transition from radial to axial-with-defect in this same range. Note that the numerically calculated curves from Ref. [24] assume fixed ratios of elastic constants, specifically  $K_{33}/K_{11} = 1$  and  $K_{22} \gg K_{11}$ . For 5CB,  $K_{33}/K_{11} \approx 1.3$  and  $K_{22}$  is smaller than both  $K_{11}$  and  $K_{33}$  [37,38]. In addition, Ref. [24] finds that  $K_{24}$  strongly influences the stability curves but only investigates two possible cases:  $K_{24} = 0$  (shown in Fig. 7) and  $K_{24} = K_{11}$ . The  $K_{24}$  value of 5CB may differ from these values, leading to altered stability regions.

Finally, our use of critical field models to estimate anchoring strength at the NLC droplet interface yield anchoring



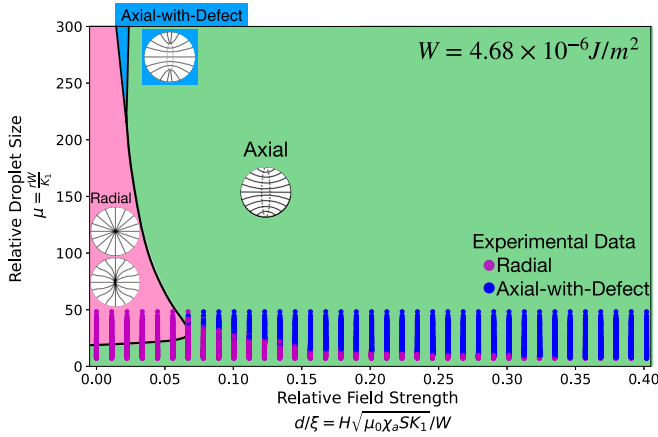


FIG. 7. Phase diagram from Ref. [24] reproduced with color indicating the three regions of stability: radial (pink), axial-with-defect (blue), and axial (green), with respect to the dimensionless parameters: relative droplet size ( $\mu = rW/K_{11}$ ) and relative field strength ( $d/\xi = H\sqrt{\mu_0\chi_aSK_{11}}/W$ ). Overlaid magenta and dark blue points illustrate our phase diagram from experimental data, showing the stability of the radial and axial-with-defect configuration states, respectively. Here we use  $W = 4.68 \times 10^{-6} \text{ J/m}^2$ , the average anchoring strength value derived from the Freedericksz transition model in Sec. VII. Note that the pink region and magenta points represent a configuration with a point defect and encompass both the radial and deformed radial configurations.

strengths in the range of  $1 - 5 \times 10^{-6} \text{ J/m}^2$  for SDS, SHS, and nTAB surfactants at 5–60% CMC. This is well within the range of previous measurements performed in a planar geometry [44–46]. In contrast to previous studies [44], within statistical error, we do not observe a trend with surfactant concentration or interfacial coverage. However, our experiments uniquely study spherical geometries rather than a planar interface. Since very few anchoring strength measurements at NLC-aqueous interfaces in suspension have been reported, our experimental work provides useful information about anchoring strengths of frequently used concentrations of SDS, SHS, and nTAB in common dispersion conditions. Further discussion of anchoring strength measurements is provided in Appendix C.

## IX. CONCLUSION

In total, this study elucidates the relationship between magnetic energy, bulk elastic energy, and surface anchoring energy in NLC droplets with homeotropic anchoring. The magnetic-field-driven configuration transition in a droplet differs fundamentally from the traditional magnetic Freedericksz transition in a rectangular cell due to the presence of a geometrically enforced topological defect. Furthermore, the study of this basic phenomenon using a magnetic field avoids inhomogeneous local fields produced by applied electric fields, thus offering a clean comparison to theory, i.e., without complex correction terms or unconfirmed assumptions. Indeed, comparison of electric versus magnetic field responses holds potential to reveal the effects of bound and free charge motions in LCs that arise in electric fields. Ultimately, we anticipate that the insights gained will be use-

ful for the design of functional soft materials that employ switchable director configurations, including magnetic-field-driven transitions in confined LC structures that favor bend or twist deformation, as well as transitions sensitive to anchoring conditions and/or topology.

## ACKNOWLEDGMENTS

This work was supported by the NSF through Grant No. DMR-2003659 and the NSF Penn Materials Research Science and Engineering Center through Grant No. DMR-1720530, including its Optical Microscopy Shared Experimental Facility. We thank Carrie Davis for assistance with the analytical calculation of the expanding ring model, Michio Tanaka for development of the tracking algorithm, Amish Patel and Yusheng Cai for helping us to understand surfactant behavior via molecular simulations, and Analisa Hill, Alexis de la Cotte, Daniel A. Beller, and Tom C. Lubensky for helpful discussions.

## APPENDIX A: CRITICAL FIELD IDENTIFICATION USING IMAGE SOFTWARE ANALYSIS

We found that experimental critical field measurements are best performed by eye by identifying the video frame in which the point defect transforms to a dark circle, indicative of a transition to a ring defect. This method, described in Sec. III, resulted in the most consistent identification of the critical field. However, we also explored other methods for determining critical field using image software analysis. For example, we tracked the integrated intensity in the droplet center to distinguish a transition from a bright point defect to a dark region inside a ring defect. The top row of Fig. 8 shows examples of POM data at zero field, where the drop center is marked with a red dot, and the red circle shows the defect region over which we integrate the intensity. Examples of intensity evolution data with increasing field strength for a variety of droplet sizes in SDS solution at 5% CMC are shown in Fig. 8.

In these plots, experimental intensity data (black points) are fit to a sigmoid curve (cyan curve). We select the center of the sigmoid curve as the critical field, shown at the dashed red line. Clearly, the transition point can be difficult to identify using image software analysis. The intrinsic thermal fluctuations of the nematic combined with relatively few pixels within the defect region leads to noisy data when analyzing the intensity in the vicinity of the point defect. Furthermore, the POM pattern can vary between droplets due to differences in droplet size, focal plane, and defect location within the droplet. This limits our ability to use the same image analysis method for all droplets. Finally, we discard data points for which the measured critical field is blatantly incorrect (for example, due to poor tracking, defect translation, or image artifacts such as smaller droplets passing through the optical path). The critical fields using this method for SDS samples at 5% CMC are displayed in the bottom panel of Fig. 9. We fit the data to the Freedericksz transition model, following Appendix B. These results can be contrasted with the critical field data obtained by eye, shown in the top panel of Fig. 9.

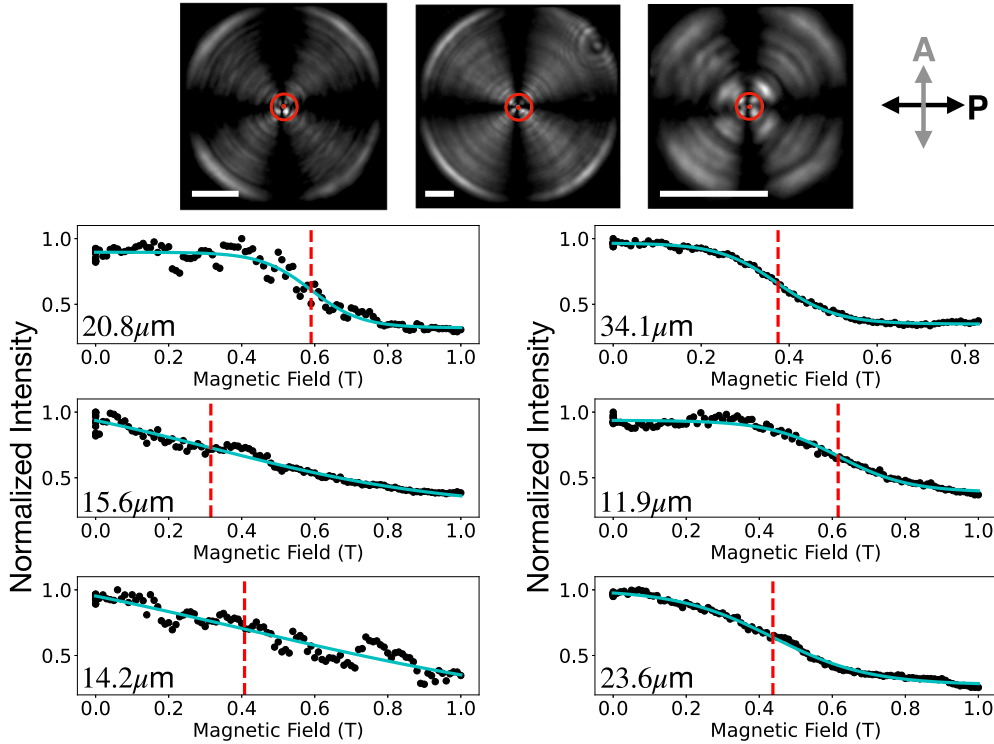


FIG. 8. The top row shows examples of POM data, where the red circle is a guide to the eye that indicates the defect region over which the intensity is integrated. The central red dot indicates the center of the droplet. The scale bar represents  $10 \mu\text{m}$  in all images. The six plots below show the intensity evolution data versus magnetic field for a variety of droplet sizes in SDS solution at 5% CMC. Experimental intensity data (black points) for individual droplets are calculated using image software. These data are fit to a sigmoid curve (cyan curve). The critical field (dashed red line) is the center of the sigmoid curve. Corresponding droplet radii are indicated on each plot.

Compared to top plot of Fig. 9, the image software data (bottom) is more scattered, and there are fewer data points. Nevertheless, we find similar anchoring strength values using both methods. Thus, although we explored many possible methods of image analysis using Python and ImageJ, including image binarization, image correlation, and a variety of integrated intensity shapes and sizes, we chose to identify the critical field by eye for our analysis. Further image analysis using other software or more sophisticated methods such as computer vision could be explored and could be useful in future studies of this nature.

We also perform image intensity analysis on the simulated POM images to obtain the plot in Fig. 10. Following the same procedure as above, we integrate the image intensity over a small sphere of radius  $r/8$  in order to observe changes in the director field configuration. We observe a discontinuous jump in intensity, indicative of a first-order transition from point to ring defect. For comparison purposes, the magnetic field strength from simulation, plotted in Fig. 10, is scaled to the experimental range using the ratio of the experimental and simulated droplet radii (details provided in Sec. IV).

## APPENDIX B: CRITICAL FIELD MODELS

### 1. Freedericksz transition model

Recall the classic Freedericksz transition result for a uniform NLC between parallel substrates in a magnetic field:

$H_c = \frac{\pi}{d} \sqrt{\frac{K}{\chi_a}}$ . Here  $d$  is the NLC thickness (substrate separation),  $K$  is the elastic constant corresponding to the field-induced distortion, and  $\chi_a$  is the magnetic anisotropy of 5CB. Our experiments differ from the classic system in three notable ways. First, this equation assumes infinite anchoring strength; our system has a finite anchoring strength at the NLC-aqueous interface. Second, this equation is derived for a planar geometry, while our droplets have a spherical geometry. Finally, while the magnetic transition in a planar cell occurs at a true Freedericksz threshold, the point-to-ring defect transition in a droplet does not. Rather, the director field of the droplet gradually distorts below the critical field  $H_c$  without a threshold, and therefore the point-to-ring transition represents a second transformation of the director configuration.

Nevertheless, we adapt the Freedericksz transition equation for our system following Ref. [44]. Weak anchoring conditions are modelled by introducing extrapolation length,  $d_e = K/W$ , such that the NLC droplet thickness is extended by  $d_e$ . This approach introduces a new surface with perfect homeotropic anchoring at thickness  $d + d_e$ , so that  $<90^\circ$  anchoring occurs at thickness  $d$ . To adapt to the spherical geometry of our system, we replace cell thickness  $d$  with  $r$ , the droplet radius. We also introduce a constant  $A$ , such that  $\pi$  becomes  $A\pi$ , where  $A > 1$ . These parameters thus adjust the original Freedericksz transition equation to account for a nonplanar geometry and to account for the fact that the point-to-ring transition occurs above the Freedericksz

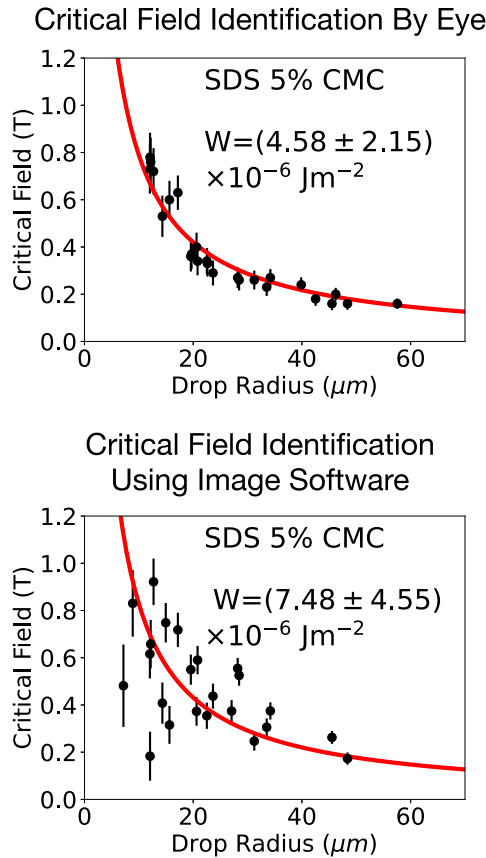


FIG. 9. Experimentally observed critical field values are shown versus drop radius using two different methods: identification by eye (top) and using image software analysis (bottom) for SDS at 5% CMC. The data are fit to the Freedericksz transition model as described in Appendix B, using the equation  $H_c = [A\pi/(r + K/W)]\sqrt{K/\chi_a}$ , where  $A = 1.28$ ,  $K = K_{11} = 6.4$  pN,  $\chi_a = 1.56 \times 10^{-6}$ , and  $W$  is a fitting parameter. The fit curve is shown in red. The calculated anchoring strength for each sample is reported on each plot.

threshold field. We assume  $A$  is constant for all droplets (assuming a spherically symmetric interface for all droplets), similarly to the geometric constant used in Ref. [16].

With these modifications, the critical field equation becomes

$$H_c = \frac{A\pi}{r + K/W} \sqrt{K/\chi_a}. \quad (\text{B1})$$

We fit all of our critical field and droplet radius data to this equation using  $K = K_{11} = 6.4$  pN [37] and  $\chi_a = 1.6 \times 10^{-6}$  [47]. These results are presented in Fig. 11. The anchoring strength,  $W$ , is a fitting parameter. For the fitting, we assume  $K$ ,  $\chi_a$ , and  $A$  are constant for all droplets, and we allow  $W$  to vary with surfactant type. The resulting data and fits are shown in Table I for each surfactant type and concentration. Uncertainty in these measurements arises from the uncertainty on  $H_c$  using our critical field identification method. This uncertainty is on average  $\pm 0.05$  T and decreases with increasing droplet size. To find the optimal  $A$ , we test  $A$  values between 1 and 3 with a step size of 0.1 and calculate the reduced chi-squared value,  $\chi_v^2$ , for each data set and  $A$  value pairing. We choose

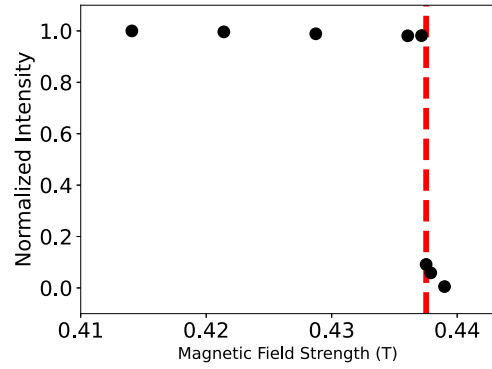


FIG. 10. Image intensity analysis of simulated POM images. The intensity is integrated over a small sphere of radius  $r/8$  for increasing magnetic field strengths. Red dashed line indicates critical field. The discontinuous jump in intensity, and consequently, director field orientation, is indicative of a first-order transition.

the  $A$  value that minimizes  $\chi_v^2$  for all data. For our data, we find the optimal  $A = 1.28$ . We can then obtain a measurement of anchoring strength,  $W$ , for each fit.

Anchoring strength measurements for SDS, SHS, and nTAB using both the Freedericksz transition model and the saturation field model are reported in Table I. These results provide a range of anchoring strength values given the measured uncertainty in the magnetic field. The analysis reveals the following conclusions: (1) We do not observe statistically significant trends with respect to surfactant concentration or chain length. (2) Within fitting errors, SDS, SHS, and nTAB surfactants have similar anchoring strengths, with a weighted average value of  $4.68 \times 10^{-6}$  J/m<sup>2</sup>. A collapse of all experimentally measured critical field data points, for all surfactants and concentrations, is shown in Fig. 6. The overall collapse onto a single curve highlights our conclusion that SDS, SHS, and nTAB have similar anchoring strengths.

## 2. Saturation field model

In addition to the Freedericksz transition model, we also explore a saturation field model to quantify the relationship between critical magnetic field, droplet radius,  $r$ , and anchoring strength,  $W$ . This second model uses the saturation field equation for weak boundary conditions, as proposed by Nehring *et al.* in Ref. [43] for a slab of NLC in an electric field. For a uniform sample of NLC confined between two parallel substrates, the saturation threshold is defined as the field at which the nematic becomes maximally aligned with the applied *electric* field. Following Ref. [43], the equation for the saturation field is  $\lambda h'' = \coth \frac{1}{2} \pi h''$ . Here  $h''$  is the reduced saturation field, defined by  $h'' = U/U_0$ , where  $U$  is the applied voltage and  $U_0$  is the threshold voltage for rigid boundary coupling or infinite anchoring. For our experiments with a *magnetic* field,  $h'' = H_c/H_0$ , where  $H_c$  is the critical magnetic field strength and  $H_0$  is the threshold field for infinite anchoring, so  $H_0 = Kd/\chi_a$ .  $\lambda$  is a reduced surface-coupling parameter defined by  $\lambda = \pi K/Wd$ .

Unlike the Freedericksz transition method, the Nehring approach is an exact solution for weak surface anchoring, based on the Rapini-Papoular theory of weak anchoring.

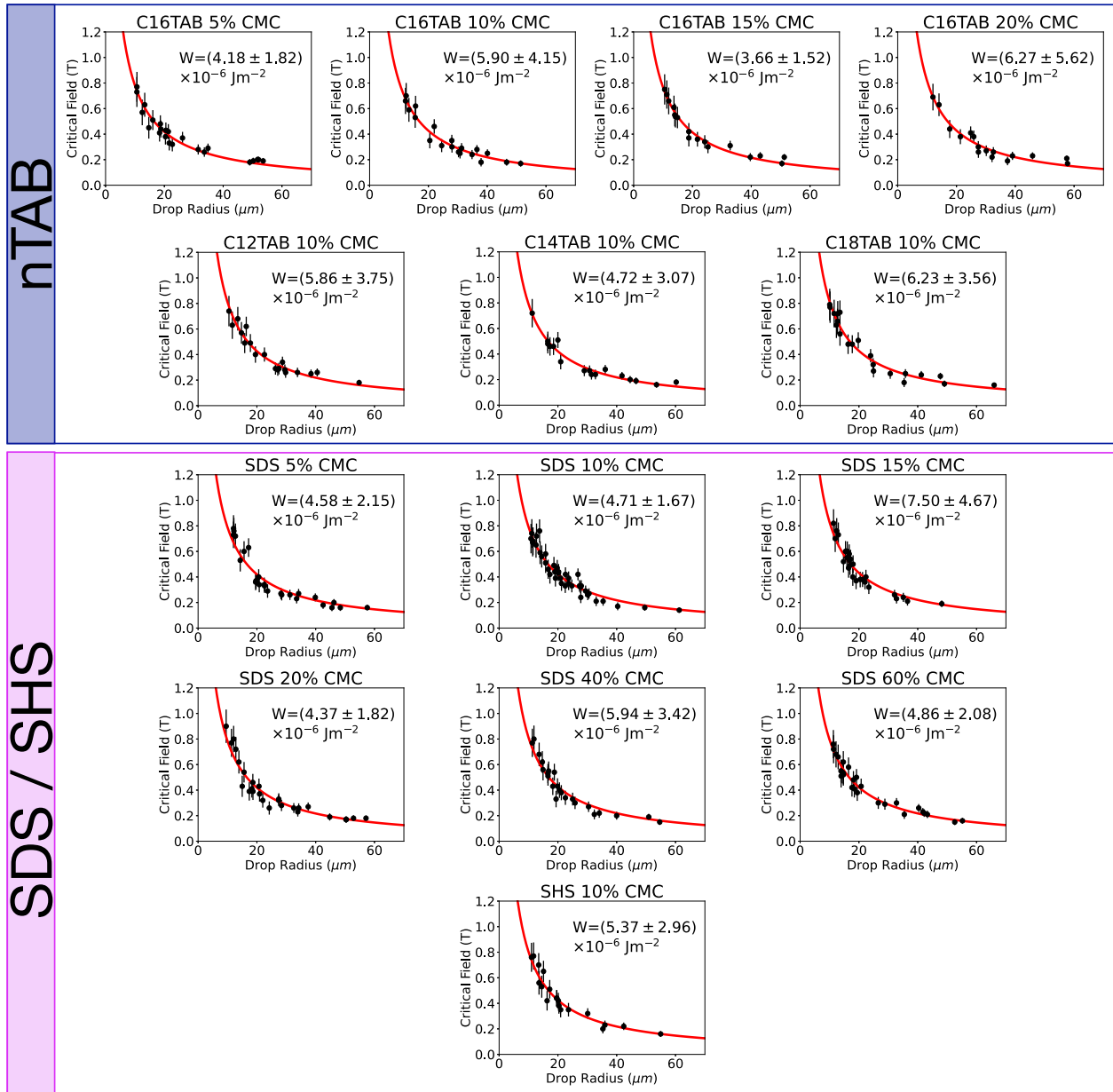


FIG. 11. Experimentally observed critical field measurements are versus drop radius for all surfactant chain lengths and concentrations. The error bars are based on uncertainty in  $H_c$  using our critical field identification method described in Sec. III. The data are fit to the Freedericksz transition model as described in Appendix B, using the equation  $H_c = [A\pi/(r + K/W)]\sqrt{K/\chi_a}$ , where  $A = 1.28$ ,  $K = K_{11} = 6.4$  pN,  $\chi_a = 1.56 \times 10^{-6}$ , and  $W$  is a fitting parameter. The fit curve is shown in red. The calculated anchoring strength for each sample is reported on each plot.

Furthermore, it accurately models the secondary nature of the transition, since both the Nehring saturation threshold and the point-to-ring transition occur at higher fields than the Freedericksz transition. However, the solution is only exact for a planar substrate geometry. Here we adapt the equation for a spherical geometry by replacing cell thickness  $d$  with droplet radius,  $r$ . Note that the spherical geometry of our system creates a complex coupling between surface boundary conditions and magnetic field, which is not fully captured by a planar model. With these caveats, we analyze the point-to-ring transition using this simplified, well-studied model to obtain an estimate for anchoring strength.

We input our data for critical field and radius into the Nehring solution and compute the anchoring strength value that minimizes the equation for all data points. Resultant anchoring strengths are shown in Table I for different surfactant concentrations and chain lengths for SDS and nTAB. As with the Freedericksz transition model, we do not observe statistically significant trends with respect to either surfactant concentration or chain length. The error bars originate from the uncertainty of  $H_c$ , which is on average  $\pm 0.05$  T and decreases with increasing droplet size. We find that SDS and nTAB surfactants have comparable anchoring strengths; their weighted average is  $1.30 \times 10^{-6} \text{ J/m}^2$ .

**APPENDIX C: DISCUSSION OF ANCHORING STRENGTH**

We employed two methods to model the relationship between critical field and droplet radius and both gave similar measurements and trends for surface anchoring strength. Previous studies of the magnetic Fredericksz transition at an NLC-aqueous interface found that anchoring strength increases with surfactant concentration and interfacial coverage [44]. By contrast, within our statistical error, we do not observe a trend with surfactant concentration.

However, it is important to note that the previous experiments differ from ours in significant ways. First, our study estimates anchoring strength using conditions typical for 5CB experiments, without added acid or salt, while the cited work uses an aqueous phase with a pH of 2 and a salt concentration of 0.1 M to modify the electrostatic repulsion and hydrophobic forces of the surfactant. Additionally, to achieve consistent interfacial excess concentrations for all surfactants, we chose the concentration of each sample to be the same

fraction of each surfactant's critical micelle concentration (CMC). Although this approach approximately enforces a similar interfacial excess energy for each surfactant, there is still inherent uncertainty in the interfacial concentration. Inconsistent interfacial excess concentrations could lead to differences in anchoring strength trends. Regardless, even though we do not observe the same trends with surfactant concentration and chain length as in prior work, our anchoring strength measurements range from  $1\text{--}5 \times 10^{-6} \text{J/m}^2$ , which is well within the range of previous measurements [44–46]. As noted above, the first two of these studies use a 0.1 M background salt concentration and 0.01 M sulfuric acid in the aqueous phase, and the third uses a 0.3 M background salt concentration. Especially since very few anchoring strength measurements at NLC-aqueous interfaces directly in suspension have been published, our work provides useful experimental information about the anchoring strengths of frequently used concentrations of SDS, SHS, and nTAB under common dispersion conditions.

- 
- [1] O. D. Lavrentovich, *Liq. Cryst.* **24**, 117 (1998).  
 [2] J. H. Erdmann, S. Žumer, and J. W. Doane, *Phys. Rev. Lett.* **64**, 1907 (1990).  
 [3] M. Kanke and K. Sasaki, *J. Phys. Soc. Jpn.* **82**, 094605 (2013).  
 [4] O. D. Lavrentovich and E. M. Terent'ev, *Zh. Eksp. Teor. Fiz.* **91**, 2084 (1986) [*Sov. Phys. JETP* **64**, 1237 (1986)].  
 [5] E. C. Gartland and S. Mkaddem, *Phys. Rev. E* **59**, 563 (1999).  
 [6] S. Mkaddem and E. C. Gartland, *Phys. Rev. E* **62**, 6694 (2000).  
 [7] P. S. Drzaic, *J. Appl. Phys.* **60**, 2142 (1986).  
 [8] J. W. Doane, A. Golemme, J. L. West, J. B. Whitehead, and B.-G. Wu, *Molec. Cryst. Liq. Cryst. Incorpor. Nonlin. Opt.* **165**, 511 (1988).  
 [9] B.-G. Wu, J. H. Erdmann, and J. W. Doane, *Liq. Cryst.* **5**, 1453 (1989).  
 [10] H. Nomura, S. Suzuki, and Y. Atarashi, *J. Appl. Phys.* **68**, 2922 (1990).  
 [11] E. M. De Groot and G. G. Fuller, *Liq. Cryst.* **23**, 113 (1997).  
 [12] A. Shabanov, V. Presnyakov, V. Zyryanov, and S. Vetrov, *Mol. Cryst. Liq. Cryst. Sci. Technol., Sect. A* **321**, 245 (1998).  
 [13] A. V. Shabanov, V. V. Presnyakov, V. Y. Zyryanov, and S. Y. Vetrov, *JETP Lett.* **67**, 733 (1998).  
 [14] F. Simoni and O. Francescangeli, *Int. J. Polym. Mater.* **45**, 381 (2000).  
 [15] P. Malik and K. Raina, *Opt. Mater. (Amst.)* **27**, 613 (2004).  
 [16] O. O. Prishchepa, A. V. Shabanov, V. Y. Zyryanov, A. M. Parshin, and V. G. Nazarov, *JETP Lett.* **84**, 607 (2007).  
 [17] A. M. Parshin, V. G. Nazarov, V. Y. Zyryanov, and V. F. Shabanov, *Mol. Cryst. Liq. Cryst.* **557**, 50 (2012).  
 [18] A. V. Koval'chuk, M. V. Kurik, O. D. Lavrentovich, and V. V. Sergan, *Zh. Eksp. Teor. Fiz.* **94**, 350 (1988) [*Sov. Phys. JETP* **67** (1988)].  
 [19] Renate Ondris-Crawford, E. P. Boyko, B. G. Wagner, J. H. Erdmann, S. Žumer, and J. W. Doane, *J. Appl. Phys.* **69**, 6380 (1991).  
 [20] V. G. Bondar, O. D. Lavrentovich, and V. M. Pergamenschchik, *Zh. Eksp. Teor. Fiz* **101**, 111 (1992) [*Sov. Phys. JETP* **74**, 60 (1992)].  
 [21] M. Humar, *Liq. Cryst.* **43**, 1937 (2016).  
 [22] Z. Karasz, M. Máthé, P. Salamon, Á. Buka, and A. Jákli, *J. Mol. Liq.* **365**, 120177 (2022).  
 [23] M. T. Máthé, B. Farkas, L. Péter, Á. Buka, A. Jákli, and P. Salamon, *Sci. Rep.* **13**, 6981 (2023).  
 [24] S. Kralj and S. Žumer, *Phys. Rev. A* **45**, 2461 (1992).  
 [25] E. M. Terentjev, *Phys. Rev. E* **51**, 1330 (1995).  
 [26] S. Candau, P. Le Roy, and F. Debeauvais, *Mol. Cryst. Liq. Cryst.* **23**, 283 (1973).  
 [27] Y. Moroi, K. Motomura, and R. Matuura, *J. Colloid Interface Sci.* **46**, 111 (1974).  
 [28] H. Kumar and G. Kaur, *J. Mol. Liq.* **298**, 111949 (2020).  
 [29] K. M. McGrath and C. J. Drummond, *Colloid Polym. Sci.* **274**, 316 (1996).  
 [30] C. C. Ruiz and J. Aguiar, *Langmuir* **16**, 7946 (2000).  
 [31] P. Mukerjee and K. J. Pasupati, *NSRDS-NBS* **36**, 66 (1971).  
 [32] M. Ravnik and S. Žumer, *Liq. Cryst.* **36**, 1201 (2009).  
 [33] D. A. Beller, Ph.D. thesis, University of Pennsylvania, 2014.  
 [34] [www.alglib.net](http://www.alglib.net).  
 [35] D. M. Sussman and D. A. Beller, *Front. Phys.* **7**, 204 (2019).  
 [36] A. Sanchez-Castillo, M. A. Osipov, and F. Giesselmann, *Phys. Rev. E* **81**, 021707 (2010).  
 [37] M. Bradshaw, E. Raynes, J. Bunning, and T. Faber, *J. Phys.* **46**, 1513 (1985).  
 [38] T. Toyooka, G.-p. Chen, H. Takezoe, and A. Fukuda, *Jpn. J. Appl. Phys.* **26**, 1959 (1987).  
 [39] A. Rapini and M. Papoular, *J. Phys. Colloq.* **30**, C4 (1969).  
 [40] E. Nowinowski-Kruszelnicki, J. Kędzierski, Z. Raszewski, L. Jaroszewicz, M. Kojdecki, W. Piecek, P. Perkowski, M. Oliferczuk, E. Miszczyk, K. Ogrodnik, and P. Morawiak, *Opto-Electr. Rev.* **20**, 255 (2012).

- [41] R.-P. Pan, T.-R. Tsai, C.-Y. Chen, and C.-L. Pan, *J. Biol. Phys.* **29**, 335 (2003).
- [42] P. S. Drzaic, *Liquid Crystal Dispersions* (World Scientific, Singapore, 1995).
- [43] J. Nehring, A. R. Kmetz, and T. J. Scheffer, *J. Appl. Phys.* **47**, 850 (1976).
- [44] F. Yesil, M. Suwa, and S. Tsukahara, *Langmuir* **34**, 81 (2018).
- [45] F. Yesil, Ph.D. thesis, Osaka University, 2017.
- [46] S. Roh, M. Tsuei, and N. L. Abbott, *Langmuir* **37**, 5810 (2021).
- [47] A. Mertelj, D. Lisjak, M. Drofenik, and M. Čopič, *Nature (Lond.)* **504**, 237 (2013).